Experimental Full-volume Airway Approximation for Assessing Breath-dependent Regional Aerosol Deposition

Ian R. Woodward, Yinkui Yu, and Catherine A. Fromen*,[#]
Department of Chemical and Biomolecular Engineering, University of Delaware, Newark, DE 19716

*corresponding author
cfromen@udel.edu
150 Academy St.
Newark, DE 19716
(302) 831-3649

[#] lead contact: cfromen@udel.edu

Author ORCIDs:
Woodward (0000-0003-4471-3734)
Yu (0000-0001-9682-9750)
Fromen (0000-0002-7528-0997)

Summary

Modeling aerosol dynamics in the airways is challenging, and most modern personalized *in vitro* tools consider only a single inhalation maneuver through less than 10% of the total lung volume. Here, we present an *in vitro* modeling pipeline to produce a device that preserves patient-specific upper airways while approximating deeper airways, capable of achieving total lung volumes over 7 liters. The modular system, called TIDAL, includes tunable inhalation and exhalation breathing capabilities with resting flow rates up to 30 liters per minute. We show that the TIDAL system is easily coupled with industrially and clinically relevant devices for aerosol therapeutics. Using a vibrating mesh nebulizer, we report central-to-peripheral (C:P) aerosol deposition measurements aligned with both *in vivo* and *in silico* benchmarks. These findings underscore the effectiveness of the TIDAL model in predicting airway deposition dynamics for inhalable therapeutics.

Keywords

pulmonary drug delivery, aerosol medicine, respiratory medicine, in vitro model, breathing, 3D printing, open cellular structures, lattice, scaling, computational design

The Bigger Picture

Inhalable medicine depends on delivering aerosols to the correct location in the lungs at the correct dosage. But many factors complicate effective delivery, including drug formulation, delivery device, and patient anatomy and physiology. To help understand how inhaled aerosols deposit in the lungs, we created the TIDAL airway approximation system to serve as an adaptable model for measuring spatial aerosol deposition in the airways, which can test the administration of aerosol therapeutics under various combinations of breathing conditions, formulations, and device parameters. The modular and scalable nature of the system can help study the effect of diseases and drugs on people with different physiologies. The TIDAL system is also readily extensible, enabling future physiological features, as well as integrated testing of organ-on-a-chip-like systems.

Highlights

Full-volume 3D printed lung model with cyclical breathing capability

Modular design pipeline combines patient upper airways and approximated deep airways

Tunable breathing by interactive graphical user interface and real-time processing

Regional aerosol deposition quantified and mapped to clinical standards

eTOC Blurb

This work presents a physical platform that uses 3D printing and modular assembly to create patient-specific architecture of the upper airways and approximate deep airways with lattice filters. The TIDAL system can replicate realistic breathing maneuvers and offer personalized evaluation of regional aerosol delivery for inhalable medicine.

Introduction

Drug delivery to the lungs enables local and systemic effects through noninvasive means, making it easier and sometimes safer compared to other routes of drug administration. However, the structural complexity of the lungs presents modelling challenges for predicting dosage efficacy. Lung airways have length scales spanning from centimeters to hundreds of micrometers in a bifurcating fractal-like network, in which each airway divides into two passages smaller in length and diameter over 20-30 airway generations, with walls lined with viscous fluids, and parenchymal motion generating transient airflow throughout.[1] Aerosol therapeutics need to ensure the delivery of the drug to an affected lung site by depositing the aerosol particles on the airway surface while navigating through these complex structures. The efficacy is further complicated by interactions between patient factors, device factors, formulation factors, and clinical and regulatory landscapes. Typical industrial processes have been designed to evaluate controllable features, such as aerosol sizing and inhaler dosing, but do not include the effects from features including lung structure, breathing maneuver, and coupled biological factors.[2] Instead, standard *in vitro-in vivo* correlations (IVIVCs) have been developed from studies of airway architecture and empirical results of aerosol deposition in a limited number of subjects.[3-8] However, these IVIVCs do not suffice for all populations and conditions, contributing to limited therapeutic efficacy of aerosol medicines and variable patient outcomes.[5-7]

Improvement to IVIVCs requires advancements to *in vitro* testing approaches that can more faithfully replicate the complex airway environment and subsequent aerosol dynamics. Thanks to advances in medical imaging and additive manufacturing, the risks of patient-specific *in vivo* testing can be mitigated by digitizing and 3D printing high-fidelity airway models for *in vitro* and *in silico* aerosol studies.[9-11] But because of limitations in resolution and radiation exposure, these instances primarily consist of mouth-throat replicas and truncated airway trees.[12,13] In *in vitro* and *in silico* contexts, researchers have had to develop approaches to efficiently capture relevant lung phenomena and estimate aerosol deposition. Early numerical models considered the airways as a series of consecutive filters.[14-16] *In silico*, such approaches include individual- and multiple-path models[17,18] and 3D-1D coupled models to simulate selected segments of the full lung space.[19,20] *In vitro*, there has been the direct analogy of the lung as a series of filters or similarly as porous media.[21-24] Current additive manufacturing technology cannot feasibly create a full-range lung or airway replica, due to the range of length scales and feature orientations present in a complete lung. In some instances, the replica is connected to a device used to generate airflow (e.g., a vacuum pump or breathing simulator) at one or more outlets of the airway tree, typically in a single direction.[9,25] As a result, even these more-realistic models do not include critical functions for evaluating regional aerosol deposition.

To advance *in vitro* aerosol deposition testing approaches, we present a platform for development and collaboration in the form of a lung approximation that synthesizes the approaches of *in vitro* and *in silico* techniques, designed to be highly modular and extensible. This system, dubbed total inhaled deposition in an actuated lung (TIDAL) model (**Figure 1**), consists of patient-derived upper airways and an approximation of deeper airways, enabled by advances in additive manufacturing and 3D printed lattice structures.[26] Based on patient-specific anatomy throughout, this model includes air-conserving breath function and a tunable porous media approximation of small airways within modular lobe units, which enables quantifiable spatial aerosol deposition under bidirectional airflow and breathing maneuvers.

Results

Designing the TIDAL system

In human lungs, aerosols enter a single channel through the mouth, throat, and trachea, before reaching the first bifurcations of the airways, where deposition by impaction is most prevalent. These upper airways are the first site of contact with inhaled aerosols and greatly contribute to the structural subject-specific variations observed in aerosol deposition. Numerous studies have considered the influence of extrathoracic and tracheobronchial variation on flow profiles and aerosol deposition.[27-36] To establish an airway model that is patient-derived and generalizable, TIDAL begins with anatomically-derived upper airways taken from medical imaging. We employed the airway geometry from Zhang et al. which has been examined extensively *in vitro* and *in silico* elsewhere;[32,37-46] alternative upper airway structures could be readily adapted to the TIDAL platform using a similar approach described herein. Airway identification and dimensional analysis by PyRaabe[47,48] and the Vascular Modeling Toolkit (VMTK)[49-51] indicated that the airway tree consisted of 135 unique branches, including all of the segmental bronchi (**Figure 2A**). This airway tree did not include physiological variants such as auxiliary airways, absence, or relocation described for other patients. With this information, we generated a modular truncated upper airway retaining the size and orientation of the airways up through the five lobar bronchi, corresponding to the intermediate-level regions of the lungs (**Figure 2C**). Doing so permitted interchangeable "plug-and-play" parts to be fit to the extrathoracic region and each lobe, enabling the truncated airways to be approximated by enclosed compartments containing filtration media. Patient demographics and average dimensions of this airway tree (**Figure 2B**, **Table S1**) were similar to the model presented by Yeh and Schum,[52] and therefore the originally reported model data were used as the morphometric bases for the remaining generations used in the lobe approximation.

Modular lobe units are connected to each lobar outlet of the upper airway model, aggregating the properties of distal airways. Earlier *in silico* models of aerosol deposition have considered a 1D model, commonly referred to as the "trumpet model", which combines the airways in each generation (i.e. level of bifurcation) to form a linear path of concentric circles along the length of the airway tree, such that every circle has a cross-sectional area equal to the total cross section of the airways in the corresponding generation.[53] The hypothetical construct resembles a horn or bell of a trumpet, having equivalent air velocity, diffusion properties, and particle filtration.[53-55] Taking this approach, each lobe, i.e. right upper (RU), right middle (RM), right lower (RL), left upper (LU), and left lower (LL), was converted to a unique horn shell design with an enclosed flexible end unit for generating airflow (**Figure 3A**).

To physically realize the particle properties, we considered 3D printed lattices, which are typically used in structural applications, as a tunable network of pores and cylinders for airflow and filtration. 3D printed lattices achieve regular structure with near-arbitrary geometry, enabling *a priori* design selection to achieve geometric properties like porosity (relative void space) and surface area. The ratio of these quantities specifies the hydraulic diameter (d_h), or the dimension of an equivalent tube in fluid applications. The hydraulic diameter is directly analogous to the airway diameter for a given generation. Therefore, by choosing lattice properties to match d_h and scaling the horn shell, the lobe approximation implicitly maintains characteristic dimensions such as the surface area-to-volume ratio and local air velocity.

Ideally, the lobe approximation process considers each airway generation in aggregate, selecting a single lattice configuration for each region and yielding equivalent geometric properties, fluid characteristics, and filtration efficiency for every combination of lobe and generation. In reality, the filtration efficiency of a generation is a complex function of multiple factors, including breathing maneuver, airway orientation, and aerosol composition. Further, not all lattice configurations are physically realizable.[26] In printability testing, we evaluated the Weaire-Phelan unit cell structure[56] (**Figure 3A**) for a number of combinations of cell length (l_c) and strut radius (r), on account of its foam likeness and pore density, which facilitated property alignment and computation (**Figures S1** and **S2**). However, after developing approaches to print fine lattices at unprecedented large scales on the order of 120 mm overall diameter, we found that this scale and configuration was not conducive to resin removal in post-processing, limiting the available lattice design space.

To facilitate the design and processing lifecycle, we applied a constraint cascade to the lobe approximation, starting with a lattice selected to have 50 ± 15% porosity, which would enable a single overall lobe shell structure to accommodate both the print resources available and a range of lattice designs, without updates to the shell. As shown previously,[57] constraining porosity also constrains the dimensionless radius ($r^* = r / l_c$) for a given unit cell design, leaving unit cell edge length as a degree of freedom to tune hydraulic diameter and making the design space more manageable. Because of print and file size constraints, the diameter of the full 3D horn structure had to be truncated (**Figure 3A**). We applied truncation to the shell at a point corresponding roughly to the transition between inertia-dominant deposition to sedimentation- and diffusion-dominant deposition mechanisms, where alveoli begin to appear along the airway walls at approximately generation 15 (G15).[58] In this constrained lobe structure, two lattice regions were designed corresponding to printable ranges and clinical regions of interest, i.e. central and peripheral deposition zones (**Figure 3A**). The central lattice region spanned airway branch generations 3-8 (G3-G8) on average, for a nominal average d_h = 5 mm; the peripheral lattice occupied the remaining generations of each lobe, with nominal average d_h = 1 mm. Further relevant quantities and parameters for each lobe are shown in **Tables S2-S7**.

To highlight the modularity of the lattice approximation, we designed two central lattice configurations for each lobe (**Figure 4**). One design used a constant beam thickness throughout the lattice structure ("uniform", **Figure 4A, right**), aligned with the target average d_h for each lobe based on single-cell calculation of r^* = 0.09 and nominal l_c = 13 mm. However, it has been shown for configurations where the overall diameter is close to the unit cell size, constrictions cause geometric properties to deviate from single-cell predictions.[57] To limit constriction at the lobe entrances, we designed another structure with a thickness gradient along the generational axis of the horn structure ("graded", **Figure 4A, left**), creating thinner elements at the entrance by applying a thickness gradient from r^* = 0.03-0.09 linearly along the length of the central lattice region. The graded central lattices are more open and closer to the average morphometric dimensions for the corresponding generations (**Figure 4B**). The peripheral lattice region and configuration were selected based on the design parameters that gave the finest repeatable prints (r = 0.2 mm, l_c = 2.3 mm). X-ray microcomputed tomography (CT) confirmed that quarter-sectioned peripheral lattice layers produced resolved pores after post-processing (**Figure 3C**), and all lattice parts were determined to have reasonable dimensional fidelity based on part mass (**Figure 3D**). The complete 3D printed parts of the LL are shown in **Figure 3E**; when fitted with an upper airway, these components can be used as a modular reduced model (**Figure 3F**).

In terms of geometric quantities between the approximation and tabular morphometric data, the total design surface area of the lobe approximation aligned with the model airway values but deviates dramatically in alveolated regions on account of the fine surface features of the lung, which are designed to facilitate oxygen and carbon dioxide exchange over an area greater than 100 m^2.[1] Such fine features, however, exceed the resolution accessible to this process. The total TIDAL design volume is on the order of 7 liters, greater than the 5.4 liters of the measured adult basis (**Figure 3B)**. This excess resulted from the design simplification of using identical silicone shells to approximate the alveolar volume of all the right upper and lower and left upper and lower lobes. Based on this agreement and visual inspection, the lattice parts were deemed suitable for assembly into the complete airway approximation.

Constructing the experimental TIDAL system to generate breathing maneuvers

We assembled over 250 components comprising the full TIDAL system, which includes the upper airways, five lobe approximation units, motion-related hardware, control software, and a modular frame enclosed within a chamber connected to the building exhaust system (**Figure 1**). We augmented the upper airway with attachments at the mouth, including a flow meter, nebulizer, and non-rebreathing valve (NRBV; **Figure 2C**). To enable bidirectional breathing capability, we implemented motion control of each individual lobe via a serial communication protocol with an Arduino MEGA microcontroller board, a Python application programming interface (API) layer, and a graphical user interface (GUI) layer. Using the GUI (**Figure 1**), users can prescribe a control curve for each lobe's inhalation and exhalation maneuver. With lattices populating each lobe unit, we evaluated the influence of the motion control parameters in producing physiologically relevant breath volumes and airflow rates (**Figure 5A-D**).

Identical parameters were assigned to inhalation and exhalation, equal for all lobes. The rate of motion was varied within the bounds of motor speed, and motion extent was varied to create a set of four test conditions, dubbed fast-tidal, fast-moderate, resting-tidal, and resting-moderate breathing. Resting breath times were longer, ranging from approximately 7-13 breaths per minute, compared to the fast conditions, which ranged from 26-45 breaths per minute, approaching hyperphysiological levels. Because of high measurement variability in the reverse-flow direction, as indicated by the flow meter manufacturer, only inhalation breathing quantities were analyzed further. In terms of inhalation flow rate, the greatest magnitude was achieved by the fast-moderate condition (26 SLPM), with the least from the resting-tidal (15 SLPM). Although average flow rate (Q_{avg}) was higher for the fast inhalation conditions, average flow rate did not show meaningful differences for either breathing rate when shifting between tidal to moderate breath extent (**Figure 5E**). Tidal volume (TV) varied from 460±3 - 860±2 mL for resting breathing, compared to 180±4 - 350±9 mL for fast breathing, highlighting the complexity of breathing dynamics in the system and the capacity to generate a range of conditions (**Figure 5F**).

Testing the TIDAL system to map aerosol deposition

To test the aerosol deposition quantification capabilities of the TIDAL system and probe the influence of lattice design, we dosed aerosols to the system under breathing conditions for two central lattice designs: beams with graded thickness and beams with uniform thickness (**Figures**

4A, 6). Selecting a representative benchmark case for aerosol deposition is complicated by the coupling of patient morphology and behavior, formulation, delivery method, and measurement technique. For this reason, Conway *et al.* published a series of studies which evaluated a number of patient-specific parameters in humans, controlling the *in vivo* aerosol administration and inhalation parameters.[59] In line with their study, we dosed liquid aerosol particles at the mouth of the model, using an Aerogen vibrating mesh nebulizer. These particles were generated from a solution of rhodamine B fluorescent dye, and the resulting cloud was measured to have a volume median diameter (VMD) of 6.77 μm with moderate variability (geometric mean diameter 4.51 μm and geometric standard deviation 2.25, **Figures S3-S4**). Rhodamine B was recovered from the part with high fidelity in washed parts with no impact on lattice mass (**Figure S5**) and residual rhodamine B was successfully removed following deposition studies with additional wash steps within a tolerance of <3%. In addition to benchmarking purposes, the selection of this aerosol formulation arose from the primary considerations of aligning device type with breathing exertion generated by the lung system, limiting particle bounce associated with solid particles, and enabling downstream analysis without necessity of radio-based techniques. Quantification of rhodamine B was determined through fluorescence measurements and reported in spatial maps of each TIDAL region (**Figure 6A**).

We delivered the aerosols for two breath extents, targeting a maximum inhalation flow rate of 18 SLPM and an inhalation volume of 600 mL or 1000 mL, respectively described as shallow or deep breathing that aligned with Conway *et al.* protocol. **Table 1** shows a summary of breathing and deposition data for shallow and deep breathing with the graded central lattice design (**Figure 6B, C**). For both conditions, over half of the deposited dose was collected from the upper airways and extrathoracic region, and deposition was slightly increased in lower lobes compared to upper lobes. Central and peripheral contributions to lobar deposition are shown in **Figure 6** maps, indicating relatively greater peripheral deposition than central deposition for each lobe.

To validate these results, we compared them to three benchmark cases under similar exposure conditions, at different levels of resolution: individual lobes, standard compartmental regions, and overall lung regions from *in vivo* standards. The multiple path particle dosimetry (MPPD)[60,61] model predicts the percentage of the deposited dose between each lobe as approximately the following: 7% RU, 3% RM, 14% RL, 7% LU, 14% LL, yielding an L:R ratio of 0.85. Increased breath volume yields a ~7% increase in predicted total deposited dose but negligible change in the distribution between lobes. While the TIDAL system deviates in lobar trends between each side of the lungs, the overall deposited dose fractions are comparable to the MPPD model predictions. The standard compartmental lung model benchmark was provided by KDEP[62], an open-source offering of the International Commission on Radiological Protection (ICRP) model.[15,16] KDEP and ICRP Publication 66 report broad regional trends based on extrathoracic, bronchial, bronchiolar, and alveolar deposition compartments. [15,16] In terms of the deposited dose, KDEP predicts a cumulative 71% in the nose, mouth, and upper respiratory region, 5% in the bronchial compartment, 5% in the bronchiolar compartment, and 18% in the alveolar compartment. Based on the corresponding generations, the central lattice region of the TIDAL model is analogous to the bronchial compartment, and the peripheral lattice region is analogous to the combination of the bronchiolar and alveolar compartments. Although the TIDAL estimate of bronchial deposition (30%) exceeds the KDEP prediction, the TIDAL model collected 23-35% of the deposited dose in the distal lobe segments, consistent with the corresponding compartments.

Conway *et al.* reported aerosol deposition *in vivo* as the central-to-peripheral deposition ratio (C:P). These regions refer to rescaling of 2D scintigraphy data into a series of shells where signal from the inner half of shells constitutes central deposition, and signal from the outer half constitutes peripheral deposition.[59] This technique can be sensitive to the definition of each region but benefits from being broadly applicable across patient populations.[61,63,64] From the benchmark data, C:P ratios for planar analysis are expected between 1-2, and computational fluid dynamics studies additionally report nearly equal deposition between central and peripheral regions.[65] In order to better compare the deposition results from the TIDAL system, they must be remapped from the generation space of the lobe approximation to the planar space used in scintigraphy, to account for the fraction of airways in a generation that overlap into each bulk region.[60,61] After applying this operation, the planar-equivalent C:P for the graded lattice studies was 0.89±0.02 and 0.84±0.04 for shallow- and deep-breathing maneuvers, respectively, which does not indicate a statistically significant difference between these conditions ($p = 0.18$). Although slightly lower than the expected values from the *in vivo* benchmark, the experimental values of the TIDAL model are within a reasonable range of performance across the two cases.

Underscoring the modular nature of the TIDAL system, we evaluated the sensitivity to a change in lattice design by replacing the gradient-thickness central lattice with a uniform-thickness design occupying the same footprint. Results for the uniform-thickness design using the shallow breathing maneuver inputs are shown in **Figure 6D** and summarized in **Table 1**. Compared to the graded central lattice design, which is more open at the entrance of each lobe approximation, the TIDAL model in this configuration showed greater deposition in the central region and in the left lobes. The planar-equivalent C:P ratio for the uniform central lattice design was 1.08 ± 0.03, which was statistically significantly different from the graded central lattice design ($p < 0.01$). In relation to the three benchmark cases, the uniform central lattice design shows results more similar to the MPPD prediction in the left lobes, compared to the graded design. The shift from peripheral to central deposition results in a higher fraction of deposited dose observed in the equivalent bronchial compartment of the ICRP 66 (KDEP) model, exceeding the model prediction. Compared to the *in vivo* benchmark cases where the expected planar C:P ranges from 1-2, the TIDAL model with uniform lattice shows improved agreement with the results based on physical human evaluation.

With this array of conditions, we considered the entire system's performance, based on the emitted dose (ED, aerosol introduced to a subject) and deposited dose (DD, aerosol reaching the surface of the lungs). By the *in vivo* benchmark, up to 90% of the emitted dose is deposited in the lungs. However, as predicted by the validated KDEP and MPPD models, 70-80% ED will deposit, with 20-40% ED landing in the airways, depending on model and breathing condition. Across all TIDAL studies, deposited dose was 51 ± 11% ED, with 29 ± 4.2% ED in the airways. This TIDAL deposited dose exceeds that of the inhalation-only SimInhale *in vitro* benchmark case which reported roughly 22 ± 3% ED deposited for 4.3 μm aerosols at 15 SLPM.[66] Thus, the TIDAL model predicts lower overall dosage but relevant levels of on-target deposition for pulmonary delivery and in line with other noteworthy *in vitro* approaches. These results show that across relevant scales and under various breathing conditions, the TIDAL model can detect differences in outcomes, using a modular design that can be tuned to align with other validated models, patient data, and pathophysiology.

Discussion and Outlook

For aerosol medicine to be effective, it must reach and deposit within the appropriate regions in the lung, but the current paradigm of relying on a formulation's particle size is an incomplete indicator of *in vivo* aerosol deposition in the lung.[67] To achieve a system that captures the patient-specific variables and device interactions of pulmonary delivery, TIDAL aims for equivalence between patient and model with respect to volume, surface area, and breathing maneuver. By using computational design and additive manufacturing, we developed a pipeline for modular designs and parts based on patient data. Our patient-derived parts enable fully sealed lobe approximation units that surpass previous studies of inhalation-only maneuvers, yielding conserved air exchange during both inhalation and exhalation maneuvers. With these features, this platform addresses an unmet need in *in vitro* systems to enable the personalized study of transient aerosol deposition for a wide range of formulations, devices, administration techniques, and patient demographics.

Physiological features were considered during approximations of the lung without loss of critical elements. The upper airways are encased in cartilage and generally more rigid than the parenchymal lung tissue. Therefore, while these airways may be subject to some motion during breathing, they are mostly static,[68,69] so they may be approximated as rigid or semi-flexible, as in the TIDAL model. Furthermore, the prevalence of upper airway architecture variants is important to capture patient-specific influences to flow and deposition profiles. Despite the typical description of a regular bifurcating tree-like system, up to 25% of the population may exhibit deviance from the typical morphology and associated genetic markers, which can be associated with increased risk for COPD.[70] Such variants include the presence or absence of auxiliary airways, or even the relocation of airway branches to sites along the trachea or terminated airway paths.[71,72] Their typical orientation and range of motion may be more unique to each patient, giving rise to more subject-specific flow profiles influencing early particle deposition in the tracheobronchial region and propagating to downstream deposition profiles. This early particle deposition is also highly influenced by the dynamic glottis geometry that creates the laryngeal jet,[73] which may require additional model controls to include the transient behavior associated with various breathing maneuvers.[74] By maintaining the upper airways in this approximation, we preserve the impaction behavior likely to be seen *in vivo* from these critical upper airway features and can accommodate patient-specific features without sacrificing modularity.

The aerosol deposition qualities of the deeper airways must also be reconstituted. TIDAL leverages 3D printed porous metamaterials to provide tunable spatial filtration within each lobe unit. From previous *in vitro* studies, it was determined that filtering structures are capable of simulating upper airway structures.[19,20] Packed-bed-like structures were also able to reflect some of the sedimentation and diffusional deposition modes, although not always strictly in the same manner as the airways.[21,24] The TIDAL approximation leverages modern additive manufacturing, which has reached a point of realizing architected materials that constitute highly tunable porous media at scale, with effectively arbitrary shape. This design flexibility, coupled with the ability to make processable, open, and self-supporting structures,[26] means that a similar porous media approach may theoretically be able to achieve filtering behavior in a way that recapitulates what is observed in human subjects at a patient-specific level. As shown here, the TIDAL system transforms a concept like the computational 1D trumpet model into a physical 3D representation (**Figure 3A**). Future iterations to incorporate additional patient data and/or pathophysiology can leverage the

design of tunable 3D printed porous metamaterials to incorporate regional obstructions, deteriorations, or even structural flexibility.

The lobe unit approximation allows for TIDAL to achieve physiologically relevant breathing flow rates and overall inhalation-exhalation profiles. Breathing profiles (**Figure 5**) are within the ranges reported by the ICRP model for sitting (TV = 750 mL; 12 breaths per minute; Q_{avg} = 9 LPM) or light work (TV = 1250 mL; 20 breaths per minute; Q_{avg} = 25 LPM).[15,16] In observations of the moderate breathing extent maneuvers, the silicone shells displayed a tendency to irregularly snap back into the uncompressed hemispherical shape, which is reflected in the inhalation waveform. This phenomenon alludes to complexity in the breathing output resulting from the complex relationship between lobe geometry, position, and rate of actuation. Further refinement of the lobe unit and compressible region may help minimize this incongruity. We have facilitated adjustment of the breathing maneuvers by using Bezier control curves for inhalation and exhalation motion, through which arbitrarily complex maneuvers can be created from a small, finite number of inputs and adjusted graphically or programmatically. This enables future application of process control or machine learning techniques to tune the breathing waveforms and align with lobe-level variance during the course of breathing.[75] Moreover, such advanced controls over the inhalation-exhalation profile will enable this model to probe mechanisms of deposition during the breathing maneuver and evaluate the role of breath holds in overall deposited dose, building from computational studies in the acinar region demonstrating their significance.[76,77]

The modular TIDAL platform provides aerosol deposition assessment under physiological breathing conditions that are reasonably aligned with clinical human observations (**Figure 6**). Extensive validation of the spatial deposition results is challenged by the high variability of clinical data and the discrepancies between regional measurements and generational airway architecture. Our results for both the gradient- and constant central lattice demonstrate distinct regional deposition profiles that are consistent with Conway *et al.* and the two computational models. Our values may differ from the benchmark *in vivo* study because of differences in extrathoracic dimensions and breathing maneuvers. While the TIDAL inhalation maneuver took place over a similar length of time as the Conway *et al.* study, there was less distinction between inhalation and hold, and the flow rate varied over the course of inhalation. In contrast, the benchmark study supplied a balance stream of compressed air to artificially maintain a constant inhalation flow rate of 18 LPM. Slower inhalation, even for larger aerosol sizes, has been shown to increase lung penetration and deposition.[78] Coupled with shorter inhalation time, there would have been enhanced conditions for impaction-driven deposition at earlier generations in the benchmark study and greater aerosol deposition in the central region.

Overall, we have addressed several practical challenges in the realization of a next-generation *in vitro* platform for inhaled aerosol testing. More broadly, this work has realized accessible processes for 3D printing fine lattices at large scales and for converting between tabular airway data to CAD- and additive-manufacturing-ready formats. These developments have culminated in a first-of-its-kind self-contained airway approximation capable of cyclic volume exchange and quantifiable aerosol deposition at the scale of the human lung. We envision this model benefiting both individually tailored aerosol delivery and the development of optimized aerosol devices and strategies. Our approach facilitates a customizable model that may enable targeted delivery for individuals; however, a more immediate application likely involves use of generalized models with approved devices and formulations to guide optimal breathing maneuvers or device designs to expand inhaled products beyond current indications or with generic products. Our design and

control pipeline is openly available for collaboration, with an aim to address the gaps in preclinical tooling and improve the effectiveness of inhaled medicine. The extensibility and modularity of this airway approximation platform have the potential to further enable rapid screening of devices, equivalency testing for generic products, or investigation of motion and mucosal dynamics in the upper airways towards improving inhalable drug delivery.

Experimental Procedures

Resource Availability

Lead contact. Further information and requests for resources should be directed to and will be fulfilled by the lead contact, Catherine Fromen (cfromen@udel.edu)

Materials availability. This study did not generate new unique materials.

Data and code availability.

Geometry, breathing, and deposition data, including data processing and analysis code, have been deposited at Zenodo under the DOI 10.5281/zenodo.11122589 and are publicly available as of the date of publication.

Micro-CT and all other data reported in this paper will be shared by the lead contact upon request.

All computational geometry code has been deposited at Zenodo under the DOI 10.5281/zenodo.11110113 and is publicly available as of the date of publication.

All control software code has been deposited at Zenodo under the DOI 10.5281/zenodo.11113197 and is publicly available as of the date of publication.

Any additional information required to reanalyze the data reported in this paper is available from the lead contact upon request.

Software and computational resources

Most computation, including analysis and control methods, was performed on a standard desktop or laptop computer running Windows 10 or Ubuntu. Computational design was performed in Rhino 6 and Grasshopper (Robert McNeel & Associates) on a Windows 10 desktop with 16 GB RAM and a 2GB dedicated graphics processor as the primary device. The in-house Grasshopper plugins facilitating lattice design are available at github.com/fromenlab/LatticeTools. In some cases, a desktop with 64 GB RAM and a 4 GB dedicated graphics processor was used to expedite lattice generation or visualization. Some parts were designed in Fusion 360 (Autodesk, Inc.). JavaScript Object Notation (JSON) was used as a human- and machine-readable means of data transfer and logging in plain text format, recording results, metadata, and properties used to perform computations and generate structures. Python (3.9, Anaconda) and R (4.2) were used extensively for data processing and communications.

In-house software was developed for controlling the TIDAL system. Layers of abstraction were implemented in the system to enable control of the lung approximation without need to manually interact with the underlying components. These layers include a command protocol for controlling the motors associated with each lobe, an application programming interface (API) to enable control of the motors via Python scripting, and a graphical user interface (GUI) to enable control of the entire system without the need for code, including features for logging and real-time analysis. This architecture enhances accessibility and usability, consistent with the modular nature of the TIDAL system. The control software is available at github.com/fromenlab/tidal.

Additive manufacturing and materials

Lattice were 3D printed via vat photopolymerization on a Carbon M1 (Carbon, Inc.) in UMA 90 Black resin with 100 µm slicing resolution. Sample lattice parts were sourced from Diversified Plastics, Inc. (Minneapolis, MN) to evaluate processing steps and production scaling. Molding was done with Ecoflex 00-30 (Smooth-On, Inc.), commonly used in soft robotics applications. The mold for the right middle lobe was printed on a Creality Ender 5 S1 in PLA, while the mold for other lobes was printed in a combination of UMA 90 Black and EPU 40. All materials were processed according to manufacturer recommendations, which included one or more of: mechanically removing excess material from the part surface, spraying or immersing in isopropyl alcohol (IPA; Fisher Chemical), spraying with compressed air, centrifugal spinning, and UV exposure. Post-processed parts were left to equilibrate for 24 hours before use. After production, part mass was measured and converted to estimated volume using the manufacturer-specified solid material density. Pore clearance in lattice quarter parts was evaluated by visual inspection and X-ray micro computed tomography (micro-CT, Bruker Skyscan 1276) with nominal resolution of 20 µm.

Upper Airway

The Geometry C upper airway was obtained from Professor Yu Feng of Oklahoma State University.[42] The original model includes an idealized mouth-throat region fit to the patient-specific tracheobronchial airway model from the X-ray computed tomography (CT) scans of a healthy 47-year-old adult male, 174 cm tall and 78 kg. From the interpolated scans of a GE 64-slice scanner with resolution 512 x 512 pixels to 500 mm x 500 mm and 2.5 mm slice thickness, the airway model consists of airway branches up to at most generation 8 (G8).[37] The airway tree was characterized using a combination of the PyRaabe software program,[47] in-house modifications,[48] and additional post-processing with the Vascular Modeling Toolkit (VMTK).[49-51] A five-lobe truncated airway model, similar to that reported by Kolewe *et al.,*[44] was generated by tracing the centerline associated with each lobar bronchus and splitting the airway model at a point on the centerline. The process is included in the code supplement and as described elsewhere.[79]

Lobe approximation and lattice design

To facilitate the lung approximation production, a porosity (ε) range of 50% was selected to enable a single shell design while also facilitating interchangeability of parts. Lattice design parameters near 50% porosity fix the dimensionless radius value for a given unit cell geometry and correspond to the peak in specific surface area for a unit cell at a given cell length. Therefore, any processing effects that would cause perturbations to the dimensionless radius – undercuring or overcuring as a result of resin type, or overcuring as a result of part scale, which are not predictable *a priori* –

would result in outcomes comparable to the expected values for surface area and porosity, based on the design dimensions.

The lobe shells were designed based on use of an idealized Weaire-Phelan unit cell at r* = 0.09 (porosity, $\varepsilon \sim 0.625$) and the asymmetric morphometric model of Yeh and Schum.[52] Given the similarity between the patient details of the upper airway model in this study and the morphometric model, no additional scaling was applied to the morphometric data before generating the parts for the lung replica. For each lobe, the published tabulated data were reproduced and processed to obtain a form suitable for CAD input. The morphometric data at each generation and in each lobe were used to determine the diameter of a circle with equal area compared to each generation's cumulative cross section. As necessary, equivalent area circles were adjusted to permit lattice insertion and removal. This occurred only in the left lower lobe. The lattice porosity was used to scale the circle diameters by $\varepsilon^{-1/2}$. This was based on an ideal analogy to porous media in a pipe.

Where the lobe shell exceeded the printable area of the Carbon M1, it was truncated with consideration given to the maximum printable generation and the location of the terminal bronchioles. That generation marks the increasing presence of alveoli along the airway walls and a transition to sedimentation- and diffusion-dominant aerosol deposition mechanisms.[52,58,80] The maximum printable generation was identified as the largest generation with a scaled equivalent diameter not exceeding 140 mm, and the remaining volume of the lobe was extruded linearly, to maintain volume equivalence. The entire lobe shell was designed as a multi-part assembly and separated into multiple parts to achieve printability (**Figure 3A, 3E**). Lattice components were also sectioned and printed as partial components, due to challenges with printing lattices at full scale (**Figures 3C, S2)**.

The alveolar shell was designed based on an extrusion of the maximum printable generation. The compressible volume was designed as a hemisphere, to facilitate both multi-part printability and casting of a flexible silicone shell. To facilitate prototyping, the same mold was used for the right upper, right lower, left upper, and left lower lobes. The compressible hemisphere was designed with an inner diameter of 128 mm and wall thickness of 4 mm, the largest design that could be printed to create one half of the mold in two parts. The right middle lobe mold design used a 2 mm wall thickness and 40 mm internal diameter, scaled for the correspondingly smaller anatomical dimensions.

Lattice geometries were designed in Rhino 6 and Grasshopper as described previously.[26,57] Both the Kelvin[65,81] and Weaire-Phelan (WP)[82] geometries have been used to represent individual alveoli in other lung modeling efforts. They are relevant because both are solutions to the problem of filling space with equal-volume cells and minimal surface area, as is common in the natural arrangement of foams and analogous to efficiently distributing air volume in contact with the alveolar epithelium.[56] The WP geometry has the highest surface area density of these standard lattice geometries, which allows designs to concentrate the hydraulic diameter in a given unit cell size. Thus, for a finite number of cells, the hydraulic diameter can be minimized to approach the analogous dimensions of the airways. This also permits the design of larger unit cells as needed to achieve a target hydraulic diameter, thereby limiting the computational demand of discretizing the design space. For these reasons, the WP lattice was selected for further experimentation.

For lattice design, the lobe shell was divided into two lattice regions, central and peripheral, corresponding to relevant regions for aerosol deposition in the lung and the Conway *et al.*

benchmark study.[59] Based on the printability results shown in **Figures S1-S2**, a common unit cell configuration was selected to represent *all* peripheral regions across the five lobes. The peripheral lattice design utilized the WP geometry at a cell length 2.3 mm and strut radius 0.2 mm, based on the processability of these dimensions at part scales on the order of 120 mm diameter. The cutoff point between central and peripheral generations was selected to align the generation-averaged diameter of the airways with the hydraulic diameter of the lattice structure for the peripheral design. From there, the lattice design for the central airway was determined by identifying the lattice configuration yielding an equivalent hydraulic diameter as the generation-averaged airway diameter for the generations between the lobar bronchus and the cutoff generation, using a dimensionless radius of $r^* = 0.09$. A central lattice design was made for each lobe with a gradient thickness ranging from $r^* = 0.03$-0.09 over the height of the part. Additional part dimensions for uniform (non-graded) parts are listed in **Figure 3B** and **Table S2**.

Hardware, electronics, and environmental controls

Low-cost, easy-access materials were preferred for hardware and electronics. To support the lung replica and enclose the apparatus, an environmental chamber was constructed from T-slot strut. The chamber occupies a footprint of 0.91 m x 0.61 m x 0.61 m or 0.51 m^3 (3' x 2' x 2'; 18 ft^3) using exclusively off-the-shelf 1" T-slot strut and bracket hardware to create the frame skeleton. Within the frame, additional struts were added to support each of the motors, lobes, and upper airway parts. The motor support struts are configured to have three degrees of freedom for positioning the motor base at any point along the three main axes of the frame. With seven total degrees of freedom for each motor, the framing system is capable of accommodating any lung geometry within the footprint.

Considering system isolation to mitigate the risks of aerosol exposure in the lab environment, transparent polymer sheets were fitted to the four side walls and top of the frame, sealed with silicone sealant or electrical tape. Passthrough ports were drilled into the side walls for electrical wiring, and a mechanical exhaust system was retrofitted from a compressed air cabinet of similar overall dimensions. This system was specified to evacuate the cabinet at 80 standard cubic feet per minute (SCFM), resulting in approximately four air changes per minute when activated in this system.

NEMA 23 stepper motors (StepperOnline 23HS30-3004S) were driven by a DM542T stepper driver (StepperOnline) and controlled via an Arduino MEGA 2560 (Arduino S.r.l.). The motors were controlled via a single interrupt service routine and direct port manipulation, to send pulses with resolution on the order of microseconds and limit overlap of blocking operations which could result in motion delays. Gears were designed using Rhino/Grasshopper, based on standard parts.

Breathing profile analysis

For initial breathing studies, breathing rate was controlled by setting the motor delay uniformly at 500 or 2100 (arbitrary units) for each of the lobes, and breath extent was controlled by the number of steps relative to a "home" position. The motor delay of 500 was determined to be the lower bound of delays to produce safe motion in the system. For aerosol deposition studies, breathing maneuvers were controlled by a software version permitting Bezier curve-defined profiles. Breathing performance was confirmed before aerosol studies, using one curve for inhalation and one curve for exhalation, common to all lobes. Breathing profiles for at least five maneuvers were

recorded in standard liters per minute (SLPM) from a TSI Model 4043 flow meter (TSI, Inc.). The flow meter was aligned with the inhalation direction of flow, and exhalation flow readings were not corrected for overestimates caused by misaligned flow direction. In accordance with recommendations for spirometry provided by the American Thoracic Society and European Respiratory Society, the sampling rate on the flow meter was set to 10 ms per reading.[83] For each condition, a series of breaths was performed, and the first and last inhalation and exhalation cycles were removed from consideration so that the analyzed breaths could be considered at steady state operation. The ambient temperature for all experiments was approximately 20 °C, and relative humidity ranged between 10-50% for aerosol experiments.

Aerosol delivery and quantification

Aerosols were delivered to the model using an Aeroneb Lab Nebulizer (Aerogen), which uses a vibrating mesh to produce a cloud of liquid aerosol droplets at a flow rate of at least 0.1 mL/min. The output of the nebulizer was evaluated with a TSI 3330 Optical Particle Sizer to have volume median diameter (VMD) of 6.77 µm with geometric mean diameter 4.51 µm and geometric standard deviation 2.25 (See **Figures S3-S4** for distributions). The nebulizer was loaded with a solution of water and rhodamine B at a concentration of 5 mg/mL and run for 15 seconds before starting the breathing profile of 60 breaths over approximately 5 minutes. Additionally, an adapter was designed and printed to connect the mouth of the model to a nebulizer and a non-rebreathing valve (Series 2630, model 112416, Hans Rudolph, Inc.). The non-rebreathing valve (NRBV) separates inhaled and exhaled air, enabling quantification of the amount of aerosol exhaled in deposition studies. Upon completing the breathing profile, all parts were separated and washed using 100-200 mL of house filtered water. Deposited mass was estimated by comparing fluorescent signal to a standard curve for rhodamine B, as measured by a Cytation V plate reader (BioTek). Washing was confirmed to not have lingering adverse effects on lattice composition, as evaluated by mass change (**Figure S5**).

To convert TIDAL deposition to a planar space for comparing the central-to-peripheral deposition ratio to *in vivo* scintigraphy studies, a matrix transformation was calculated based on assigning a fraction of airway each generation to central and peripheral regions, equally splitting the intermediate zone between the two. The distribution of airways in each generation corresponding to central and peripheral regions was adapted from previous reports,[60,61] and our source code is available as referenced in the Resource Availability section. In line with calculations from Conway *et al.*, deposition in MT and TB are not included in our C:P determinations.

Acknowledgements

The authors would like to acknowledge D. Hoffman and D. Rastogi for their assistance; E. Kolewe for discussions in the course of the work; E. R. Williams and H. Kabaria from Carbon, Inc. for early discussions regarding print capabilities; and A. Woodward for discussion regarding X-ray CT scan settings. The authors would like to recognize Diversified Plastics, Inc. for services rendered in processing initial lattice quarter parts. Elements of the graphical abstract were created with BioRender.com.

Funding. This work was supported by the National Institute of General Medical Sciences of the National Institutes of Health under award R35GM142866A and the National Science Foundation

under award 2237430. I.R.W. was supported by a GAANN Fellowship funded by the Department of Education (P200A210065). Micro-CT imaging was supported by the National Institutes of Health, National Institute of General Medical Sciences COBRE (P20 GM139760). The content is solely the responsibility of the authors and does not necessarily represent the official views of the National Institutes of Health, National Science Foundation, or Department of Education.

Author contributions. I.R.W. and C.A.F. conceptualized the device and study design. I.R.W designed the lobe approximation, airway truncation, interior lattices, and environmental housing. Y.Y. designed lobe support structures. Y.Y. assembled the original single lobe chamber. I.R.W. and Y.Y. printed parts. Y.Y. performed X-ray micro-CT characterization. I.R.W. manufactured the full TIDAL and single lobe prototypes. I.R.W. designed motor controls and associated software and executed the breathing evaluations. I.R.W., Y.Y., and C.A.F. designed and performed the experimental aerosol investigations and validation. Y.Y. obtained results from MPPD and KDEP (ICRP) models. I.R.W. curated the data and prepared the data visualization. I.R.W wrote the original draft. I.R.W. and C.A.F. reviewed and edited the final manuscript. C.A.F. was responsible for project administration, funding acquisition, and supervision.

Declaration of interests. I.R.W. and C.A.F. are the inventors of a pending patent filed by University of Delaware (U.S. Patent Application Serial No.: 63/278,131).

Supplemental Information.

Supplementary document containing Figures S1–S5 and Tables S1-S7.

References

1. Hsia, C.C., Hyde, D.M., and Weibel, E.R. (2016). Lung Structure and the Intrinsic Challenges of Gas Exchange. Compr Physiol 6, 827-895, 10.1002/cphy.c150028.
2. Newman, B., and Witzmann, K. (2020). Addressing the Regulatory and Scientific Challenges with Generic Orally Inhaled Drug Products. Pharmaceut Med 34, 93-102, 10.1007/s40290-020-00327-y.
3. Patton, J.S., and Byron, P.R. (2007). Inhaling medicines: delivering drugs to the body through the lungs. Nature reviews. Drug discovery 6, 67-74, 10.1038/nrd2153.
4. Byron, P.R., Hindle, M., Lange, C.F., Longest, P.W., McRobbie, D., Oldham, M.J., Olsson, B., Thiel, C.G., Wachtel, H., and Finlay, W.H. (2010). In vivo-in vitro correlations: predicting pulmonary drug deposition from pharmaceutical aerosols. J Aerosol Med Pulm Drug Deliv 23 Suppl 2, S59-69, 10.1089/jamp.2010.0846.
5. Chow, M.Y.T., Tai, W., Chang, R.Y.K., Chan, H.-K., and Kwok, P.C.L. (2021). In vitro-in vivo correlation of cascade impactor data for orally inhaled pharmaceutical aerosols. Advanced Drug Delivery Reviews 177, 113952, https://doi.org/10.1016/j.addr.2021.113952.
6. Huang, F., Zhu, Q., Zhou, X., Gou, D., Yu, J., Li, R., Tong, Z., and Yang, R. (2021). Role of CFD based in silico modelling in establishing an in vitro-in vivo correlation of aerosol deposition in the respiratory tract. Advanced Drug Delivery Reviews 170, 369-385, https://doi.org/10.1016/j.addr.2020.09.007.
7. Newman, S.P., and Chan, H.-K. (2020). In vitro-in vivo correlations (IVIVCs) of deposition for drugs given by oral inhalation. Advanced Drug Delivery Reviews 167, 135-147, https://doi.org/10.1016/j.addr.2020.06.023.
8. Newman, B., and Witzmann, K. (2020). Addressing the Regulatory and Scientific Challenges with Generic Orally Inhaled Drug Products. Pharmaceutical Medicine 34, 93-102, 10.1007/s40290-020-00327-y.
9. Verbanck, S., Ghorbaniasl, G., Biddiscombe, M.F., Dragojlovic, D., Ricks, N., Lacor, C., Ilsen, B., de Mey, J., Schuermans, D., Underwood, S.R. et al. (2016). Inhaled Aerosol Distribution in Human Airways: A Scintigraphy-Guided Study in a 3D Printed Model. J Aerosol Med Pulm Drug Deliv 29, 525-533, 10.1089/jamp.2016.1291.
10. Nordlund, M., Belka, M., Kuczaj, A.K., Lizal, F., Jedelsky, J., Elcner, J., Jicha, M., Sauser, Y., Le Bouhellec, S., Cosandey, S. et al. (2017). Multicomponent aerosol particle deposition in a realistic cast of the human upper respiratory tract. Inhal Toxicol 29, 113-125, 10.1080/08958378.2017.1315196.
11. Lizal, F., Belka, M., Adam, J., Jedelsky, J., and Jicha, M. (2015). A method for in vitro regional aerosol deposition measurement in a model of the human tracheobronchial tree by the positron emission tomography. Proc Inst Mech Eng H 229, 750-757, 10.1177/0954411915600005.
12. de Jong, P.A., Muller, N.L., Pare, P.D., and Coxson, H.O. (2005). Computed tomographic imaging of the airways: relationship to structure and function. Eur Respir J 26, 140-152, 10.1183/09031936.05.00007105.
13. Watz, H., Barile, S., Guastalla, D., Topole, E., Cocconi, D., Mignot, B., Belmans, D., Duman, D., Poli, G., and Fabbri, L.M. (2021). Targeting the Small Airways with Inhaled Corticosteroid/Long-Acting Beta Agonist Dry Powder Inhalers: A Functional Respiratory Imaging Study. J Aerosol Med Pulm Drug Deliv 34, 280-292, 10.1089/jamp.2020.1618.

14. Hofmann, W. (2011). Modelling inhaled particle deposition in the human lung—A review. Journal of Aerosol Science 42, 693-724, 10.1016/j.jaerosci.2011.05.007.
15. Human respiratory tract model for radiological protection. (1994). 1. ed Edition (Pergamon Press).
16. Paquet, F., Etherington, G., Bailey, M.R., Leggett, R.W., Lipsztein, J., Bolch, W., Eckerman, K.F., Harrison, J.D., and Icrp (2015). ICRP Publication 130: Occupational Intakes of Radionuclides: Part 1. Ann ICRP 44, 5-188, 10.1177/0146645315577539.
17. Longest, P.W., Tian, G., Delvadia, R., and Hindle, M. (2012). Development of a Stochastic Individual Path (SIP) Model for Predicting the Deposition of Pharmaceutical Aerosols: Effects of Turbulence, Polydisperse Aerosol Size, and Evaluation of Multiple Lung Lobes. Aerosol Science and Technology 46, 1271-1285, 10.1080/02786826.2012.708799.
18. Kolanjiyil, A.V., and Kleinstreuer, C. (2017). Computational analysis of aerosol-dynamics in a human whole-lung airway model. Journal of Aerosol Science 114, 301-316, 10.1016/j.jaerosci.2017.10.001.
19. Tavernini, S., Kiaee, M., Farina, D.J., Martin, A.R., and Finlay, W.H. (2019). Development of a filter that mimics tracheobronchial deposition of respirable aerosols in humans. Aerosol Science and Technology 53, 802-816, 10.1080/02786826.2019.1606414.
20. Koehler, K.A., and Volckens, J. (2013). Development of a sampler to estimate regional deposition of aerosol in the human respiratory tract. Ann Occup Hyg 57, 1138-1147, 10.1093/annhyg/met041.
21. Gebhart, J., and Heyder, J. (1985). Removal of aerosol particles from stationary air within porous media. Journal of Aerosol Science 16, 175-187, 10.1016/0021-8502(85)90085-0.
22. Saini, D., Yurteri, C.U., Grable, N., Sims, R.A., and Mazumder, M.K. (2002). Drug delivery studies on electrostatically charged dry powder inhaler aerosols using a glass bead lung model. Conference Record of the 2002 IEEE Industry Applications Conference. 37th IAS Annual Meeting (Cat. No.02CH37344).
23. Holbrook, L.T. (2015). Generation and Delivery of Charged Aerosols to Infant Airways. (Virginia Commonwealth University).
24. Bass, K., and Longest, P.W. (2018). Development of an infant complete-airway in vitro model for evaluating aerosol deposition. Med Eng Phys, 10.1016/j.medengphy.2018.05.002.
25. Wells, B., Guest, N., Martinez, J., Hakizimana, E., April Si, X., Su, W.-C., and Xi, J. (2018). Visualization and quantification of nebulized aerosol deposition in mouth-lung casts under healthy and abnormal breathing conditions. Lungs and Breathing 2, 10.15761/lbj.1000127.
26. Woodward, I.R., and Fromen, C.A. (2021). Scalable, process-oriented beam lattices: generation, characterization, and compensation for open cellular structures. Addit Manuf 48, 102386, 10.1016/j.addma.2021.102386.
27. Grgic, B., Finlay, W.H., Burnell, P.K.P., and Heenan, A.F. (2004). In vitro intersubject and intrasubject deposition measurements in realistic mouth–throat geometries. Journal of Aerosol Science 35, 1025-1040, 10.1016/j.jaerosci.2004.03.003.

28. Golshahi, L., Noga, M.L., and Finlay, W.H. (2012). Deposition of inhaled micrometer-sized particles in oropharyngeal airway replicas of children at constant flow rates. Journal of Aerosol Science 49, 21-31, 10.1016/j.jaerosci.2012.03.001.
29. Borojeni, A.A.T., Noga, M.L., Vehring, R., and Finlay, W.H. (2014). Measurements of total aerosol deposition in intrathoracic conducting airway replicas of children. Journal of Aerosol Science 73, 39-47, 10.1016/j.jaerosci.2014.03.005.
30. Martin, A.R., Moore, C.P., and Finlay, W.H. (2018). Models of deposition, pharmacokinetics, and intersubject variability in respiratory drug delivery. Expert opinion on drug delivery 15, 1175-1188, 10.1080/17425247.2018.1544616.
31. Paxman, T., Noga, M., Finlay, W.H., and Martin, A.R. (2019). Experimental evaluation of pressure drop for flows of air and heliox through upper and central conducting airway replicas of 4- to 8-year-old children. J Biomech 82, 134-141, 10.1016/j.jbiomech.2018.10.028.
32. Feng, Y., Zhao, J., Kleinstreuer, C., Wang, Q., Wang, J., Wu, D.H., and Lin, J. (2018). An in silico inter-subject variability study of extra-thoracic morphology effects on inhaled particle transport and deposition. Journal of Aerosol Science 123, 185-207, 10.1016/j.jaerosci.2018.05.010.
33. Walenga, R.L., Longest, P.W., Kaviratna, A., and Hindle, M. (2017). Aerosol Drug Delivery During Noninvasive Positive Pressure Ventilation: Effects of Intersubject Variability and Excipient Enhanced Growth. J Aerosol Med Pulm Drug Deliv 30, 190-205, 10.1089/jamp.2016.1343.
34. Miyawaki, S., Hoffman, E.A., Wenzel, S.E., and Lin, C.L. (2019). Aerosol deposition predictions in computed tomography-derived skeletons from severe asthmatics: A feasibility study. Clin Biomech (Bristol, Avon) 66, 81-87, 10.1016/j.clinbiomech.2017.10.020.
35. Sera, T., Kuninaga, H., Fukasaku, K., Yokota, H., and Tanaka, M. (2019). The Effectiveness of An Averaged Airway Model in Predicting the Airflow and Particle Transport Through the Airway. J Aerosol Med Pulm Drug Deliv 32, 278-292, 10.1089/jamp.2018.1500.
36. Wei, X., Hindle, M., Kaviratna, A., Huynh, B.K., Delvadia, R.R., Sandell, D., and Byron, P.R. (2018). In Vitro Tests for Aerosol Deposition. VI: Realistic Testing with Different Mouth-Throat Models and In Vitro-In Vivo Correlations for a Dry Powder Inhaler, Metered Dose Inhaler, and Soft Mist Inhaler. J Aerosol Med Pulm Drug Deliv 31, 358-371, 10.1089/jamp.2018.1454.
37. Zhang, Z., Kleinstreuer, C., and Hyun, S. (2012). Size-change and deposition of conventional and composite cigarette smoke particles during inhalation in a subject-specific airway model. Journal of Aerosol Science 46, 34-52, 10.1016/j.jaerosci.2011.12.002.
38. Zhang, Z., Kleinstreuer, C., and Feng, Y. (2012). Vapor deposition during cigarette smoke inhalation in a subject-specific human airway model. Journal of Aerosol Science 53, 40-60, 10.1016/j.jaerosci.2012.05.008.
39. Banko, A.J., Coletti, F., Schiavazzi, D., Elkins, C.J., and Eaton, J.K. (2015). Three-dimensional inspiratory flow in the upper and central human airways. Experiments in Fluids 56, 10.1007/s00348-015-1966-y.

40. Banko, A.J., Coletti, F., Elkins, C.J., and Eaton, J.K. (2016). Oscillatory flow in the human airways from the mouth through several bronchial generations. International Journal of Heat and Fluid Flow 61, 45-57, 10.1016/j.ijheatfluidflow.2016.04.006.
41. Bernate, J.A., Geisler, T.S., Padhy, S., Shaqfeh, E.S.G., and Iaccarino, G. (2017). Study of the flow unsteadiness in the human airway using large eddy simulation. Physical Review Fluids 2, 10.1103/PhysRevFluids.2.083101.
42. Feng, Y., Zhao, J., Chen, X., and Lin, J. (2017). An In Silico Subject-Variability Study of Upper Airway Morphological Influence on the Airflow Regime in a Tracheobronchial Tree. Bioengineering (Basel) 4, 10.3390/bioengineering4040090.
43. Asgari, M., Lucci, F., Bialek, J., Dunan, B., Andreatta, G., Smajda, R., Lani, S., Blondiaux, N., Majeed, S., Steiner, S. et al. (2019). Development of a realistic human respiratory tract cast representing physiological thermal conditions. Aerosol Science and Technology 53, 860-870, 10.1080/02786826.2019.1612839.
44. Kolewe, E.L., Feng, Y., and Fromen, C.A. (2021). Realizing Lobe-Specific Aerosol Targeting in a 3D-Printed In Vitro Lung Model. J Aerosol Med Pulm Drug Deliv 34, 42-56, 10.1089/jamp.2019.1564.
45. Peterman, E.L., Kolewe, E.L., and Fromen, C.A. (2020). Evaluating Regional Pulmonary Deposition using Patient-Specific 3D Printed Lung Models. J Vis Exp, e61706, 10.3791/61706.
46. Sperry, T., Feng, Y., Zhao, J., Song, C., and Shi, Z. (2023). Prediction of the transport, deposition, and absorption of multicomponent E-cigarette aerosols in a subject-specific mouth-to-G10 human respiratory system. Journal of Aerosol Science 170, 106157, 10.1016/j.jaerosci.2023.106157.
47. Kuprat, A.P., Jalali, M., Jan, T., Corley, R.A., Asgharian, B., Price, O., Singh, R.K., Colby, S., and Darquenne, C. (2021). Efficient bi-directional coupling of 3D Computational Fluid-Particle Dynamics and 1D Multiple Path Particle Dosimetry lung models for multiscale modeling of aerosol dosimetry. J Aerosol Sci 151, 10.1016/j.jaerosci.2020.105647.
48. Kolewe, E.L., Padhye, S., Woodward, I.R., Wee, J., Rahman, T., Feng, Y., Briddell, J.W., and Fromen, C.A. (2022). Spatial aerosol deposition correlated to anatomic feature development in 6-year-old upper airway computational models. Comput Biol Med 149, 106058, 10.1016/j.compbiomed.2022.106058.
49. Antiga, L., and Steinman, D.A. (2004). Robust and objective decomposition and mapping of bifurcating vessels. IEEE Trans Med Imaging 23, 704-713, 10.1109/tmi.2004.826946.
50. Antiga, L., Piccinelli, M., Botti, L., Ene-Iordache, B., Remuzzi, A., and Steinman, D.A. (2008). An image-based modeling framework for patient-specific computational hemodynamics. Med Biol Eng Comput 46, 1097-1112, 10.1007/s11517-008-0420-1.
51. Izzo, R., Steinman, D., Manini, S., and Antiga, L. (2018). The Vascular Modeling Toolkit: A Python Library for the Analysis of Tubular Structures in Medical Images. Journal of Open Source Software 3, 745, 10.21105/joss.00745.
52. Yeh, H.C., and Schum, G.M. (1980). Models of human lung airways and their application to inhaled particle deposition. Bull Math Biol 42, 461-480, 10.1007/bf02460796.
53. Taulbee, D.B., and Yu, C.P. (1975). A theory of aerosol deposition in the human respiratory tract. J Appl Physiol (1985) 38, 77-85, 10.1152/jappl.1975.38.1.77.
54. Kolanjiyil, A.V., and Kleinstreuer, C. (2016). Computationally efficient analysis of particle transport and deposition in a human whole-lung-airway model. Part I: Theory

and model validation. Comput Biol Med 79, 193-204, 10.1016/j.compbiomed.2016.10.020.
55. Oakes, J.M., Shadden, S.C., Grandmont, C., and Vignon-Clementel, I.E. (2017). Aerosol transport throughout inspiration and expiration in the pulmonary airways. Int J Numer Method Biomed Eng 33, 10.1002/cnm.2847.
56. Weaire, D., and Phelan, R. (1994). A counter-example to Kelvin's conjecture on minimal surfaces. Philosophical Magazine Letters 69, 107-110, 10.1080/09500839408241577.
57. Woodward, I.R., Attia, L.M., Patel, P., and Fromen, C.A. (2021). Scalable 3D-printed lattices for pressure control in fluid applications. AIChE J 67, e17452, 10.1002/aic.17452.
58. Darquenne, C. (2012). Aerosol deposition in health and disease. J Aerosol Med Pulm Drug Deliv 25, 140-147, 10.1089/jamp.2011.0916.
59. Conway, J., Fleming, J., Majoral, C., Katz, I., Perchet, D., Peebles, C., Tossici-Bolt, L., Collier, L., Caillibotte, G., Pichelin, M. et al. (2012). Controlled, parametric, individualized, 2-D and 3-D imaging measurements of aerosol deposition in the respiratory tract of healthy human subjects for model validation. Journal of Aerosol Science 52, 1-17, https://doi.org/10.1016/j.jaerosci.2012.04.006.
60. Olsson, B., and Kassinos, S.C. (2021). On the Validation of Generational Lung Deposition Computer Models Using Planar Scintigraphic Images: The Case of Mimetikos Preludium. J Aerosol Med Pulm Drug Deliv 34, 115-123, 10.1089/jamp.2020.1620.
61. Schroeter, J.D., Pritchard, J.N., Hwang, D., and Martonen, T.B. (2005). Airway identification within planar gamma camera images using computer models of lung morphology. Pharmaceutical research 22, 1692-1699, 10.1007/s11095-005-6628-y.
62. Klumpp, J., and Bertelli, L. (2017). KDEP: A Resource for Calculating Particle Deposition in the Respiratory Tract. Health Phys 113, 110-121, 10.1097/HP.0000000000000679.
63. Conway, J. (2012). Lung imaging - two dimensional gamma scintigraphy, SPECT, CT and PET. Adv Drug Deliv Rev 64, 357-368, 10.1016/j.addr.2012.01.013.
64. Laube, B.L. (2022). Imaging Aerosol Deposition with Two-Dimensional Gamma Scintigraphy. J Aerosol Med Pulm Drug Deliv 35, 333-341, 10.1089/jamp.2022.29072.bll.
65. Tian, G., Hindle, M., Lee, S., and Longest, P.W. (2015). Validating CFD Predictions of Pharmaceutical Aerosol Deposition with In Vivo Data. Pharmaceutical research 32, 3170-3187, 10.1007/s11095-015-1695-1.
66. Koullapis, P., Kassinos, S.C., Muela, J., Perez-Segarra, C., Rigola, J., Lehmkuhl, O., Cui, Y., Sommerfeld, M., Elcner, J., Jicha, M. et al. (2018). Regional aerosol deposition in the human airways: The SimInhale benchmark case and a critical assessment of in silico methods. European Journal of Pharmaceutical Sciences 113, 77-94, https://doi.org/10.1016/j.ejps.2017.09.003.
67. Snell, N.J., and Ganderton, D. (1999). Assessing lung deposition of inhaled medications. Consensus statement from a workshop of the British Association for Lung Research, held at the Institute of Biology, London, U.K. on 17 April 1998. Respir Med 93, 123-133, 10.1016/s0954-6111(99)90302-5.
68. Zhao, J., Feng, Y., Koshiyama, K., and Wu, H. (2021). Prediction of airway deformation effect on pulmonary air-particle dynamics: A numerical study. Physics of Fluids 33, 101906, 10.1063/5.0065309.

69. Choi, J. (2011). Multiscale numerical analysis of airflow in CT-based subject specific breathing human lungs. 10.17077/etd.n7qno7h9.
70. Smith, B.M., Traboulsi, H., Austin, J.H.M., Manichaikul, A., Hoffman, E.A., Bleecker, E.R., Cardoso, W.V., Cooper, C., Couper, D.J., Dashnaw, S.M. et al. (2018). Human airway branch variation and chronic obstructive pulmonary disease. Proc Natl Acad Sci U S A 115, E974-E981, 10.1073/pnas.1715564115.
71. Chassagnon, G., Morel, B., Carpentier, E., Ducou Le Pointe, H., and Sirinelli, D. (2016). Tracheobronchial Branching Abnormalities: Lobe-based Classification Scheme. Radiographics 36, 358-373, 10.1148/rg.2016150115.
72. Martin-Ruiz, S., Gutierrez-Collar, C., Forcen Vicente De Vera, E., Bernabe-Barrios, M.J., de Blas, C.S., Konschake, M., Ramon Sanudo, J., and Maranillo, E. (2021). The bronchial segmentation and its anatomical variations. A clinical-anatomic and bronchoscopy study. Ann Anat 235, 151677, 10.1016/j.aanat.2021.151677.
73. Xi, J., Longest, P.W., and Martonen, T.B. (2008). Effects of the laryngeal jet on nano- and microparticle transport and deposition in an approximate model of the upper tracheobronchial airways. Journal of Applied Physiology 104, 1761-1777, 10.1152/japplphysiol.01233.2007.
74. Zhao, J., Feng, Y., and Fromen, C.A. (2020). Glottis motion effects on the particle transport and deposition in a subject-specific mouth-to-trachea model: A CFPD study. Computers in Biology and Medicine 116, 103532, https://doi.org/10.1016/j.compbiomed.2019.103532.
75. Jahani, N., Choi, S., Choi, J., Iyer, K., Hoffman, E.A., and Lin, C.L. (2015). Assessment of regional ventilation and deformation using 4D-CT imaging for healthy human lungs during tidal breathing. J Appl Physiol (1985) 119, 1064-1074, 10.1152/japplphysiol.00339.2015.
76. Koullapis, P.G., Hofemeier, P., Sznitman, J., and Kassinos, S.C. (2018). An efficient computational fluid-particle dynamics method to predict deposition in a simplified approximation of the deep lung. European Journal of Pharmaceutical Sciences 113, 132-144, https://doi.org/10.1016/j.ejps.2017.09.016.
77. Koullapis, P.G., Stylianou, F.S., Sznitman, J., Olsson, B., and Kassinos, S.C. (2020). Towards whole-lung simulations of aerosol deposition: A model of the deep lung. Journal of Aerosol Science 144, 105541, https://doi.org/10.1016/j.jaerosci.2020.105541.
78. Zeman, K.L., Wu, J., and Bennett, W.D. (2010). Targeting aerosolized drugs to the conducting airways using very large particles and extremely slow inhalations. J Aerosol Med Pulm Drug Deliv 23, 363-369, 10.1089/jamp.2008.0711.
79. Woodward, I.R. (2023). Additive Manufacturing and Open Lattice Structures for Applications in Chemical Engineering and Pulmonary Drug Delivery. (University of Delaware).
80. Ewald R. Weibel, M.D. (1963). Morphometry of the Human Lung. 10.1016/c2013-0-08161-3.
81. Sznitman, J., Heimsch, T., Wildhaber, J.H., Tsuda, A., and Rosgen, T. (2009). Respiratory flow phenomena and gravitational deposition in a three-dimensional space-filling model of the pulmonary acinar tree. J Biomech Eng 131, 031010, 10.1115/1.3049481.
82. Grigoryan, B., Paulsen, S.J., Corbett, D.C., Sazer, D.W., Fortin, C.L., Zaita, A.J., Greenfield, P.T., Calafat, N.J., Gounley, J.P., Ta, A.H. et al. (2019). Multivascular

networks and functional intravascular topologies within biocompatible hydrogels. Science 364, 458-464, 10.1126/science.aav9750.
83. Graham, B.L., Steenbruggen, I., Miller, M.R., Barjaktarevic, I.Z., Cooper, B.G., Hall, G.L., Hallstrand, T.S., Kaminsky, D.A., McCarthy, K., McCormack, M.C. et al. (2019). Standardization of Spirometry 2019 Update. An Official American Thoracic Society and European Respiratory Society Technical Statement. Am J Respir Crit Care Med 200, e70-e88, 10.1164/rccm.201908-1590ST.

Figures

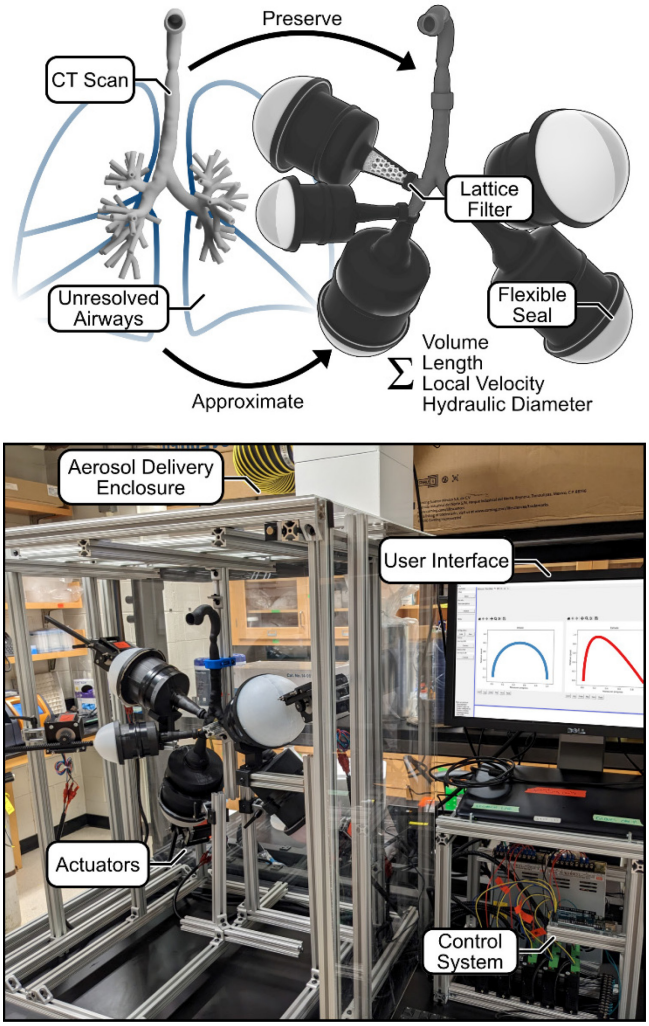

Figure 1. Overview of the TIDAL system. Patient features are preserved in the TIDAL model, and distal airways are approximated as 3D printed lattice filters by considering their cumulative regional properties. The TIDAL model is programmed with controllable breathing parameters within an enclosed aerosol delivery space. With the TIDAL system, it is possible to assess spatial aerosol deposition and account for interactions between device, formulation, and patient factors.

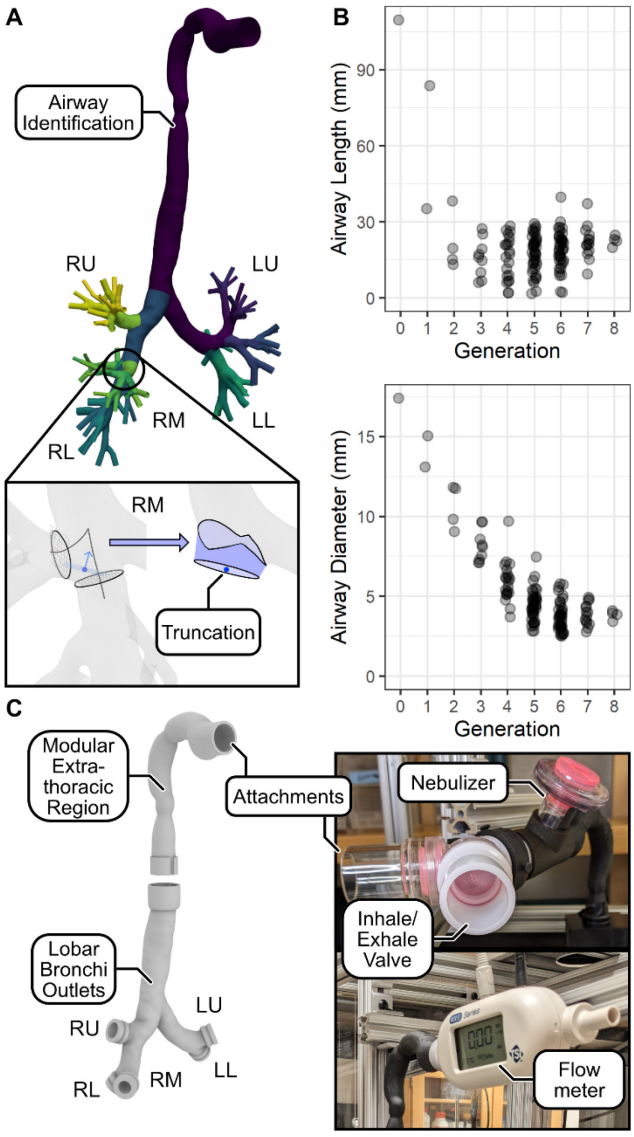

Figure 2. Upper airway features. (A) The patient-specific upper airway tree is discretized into individual branches and truncated for the TIDAL model. Shaded regions indicate unique branches. Lobe abbreviations: right upper (RU), right middle (RM), right lower (RL), left upper (LU), left lower (LL). (B) Airway length and diameter are characterized for each individual airway from the full tree geometry. (C) Truncated upper airway model with modular extrathoracic region, including idealized mouth-throat replica and device attachments. See also Table S1.

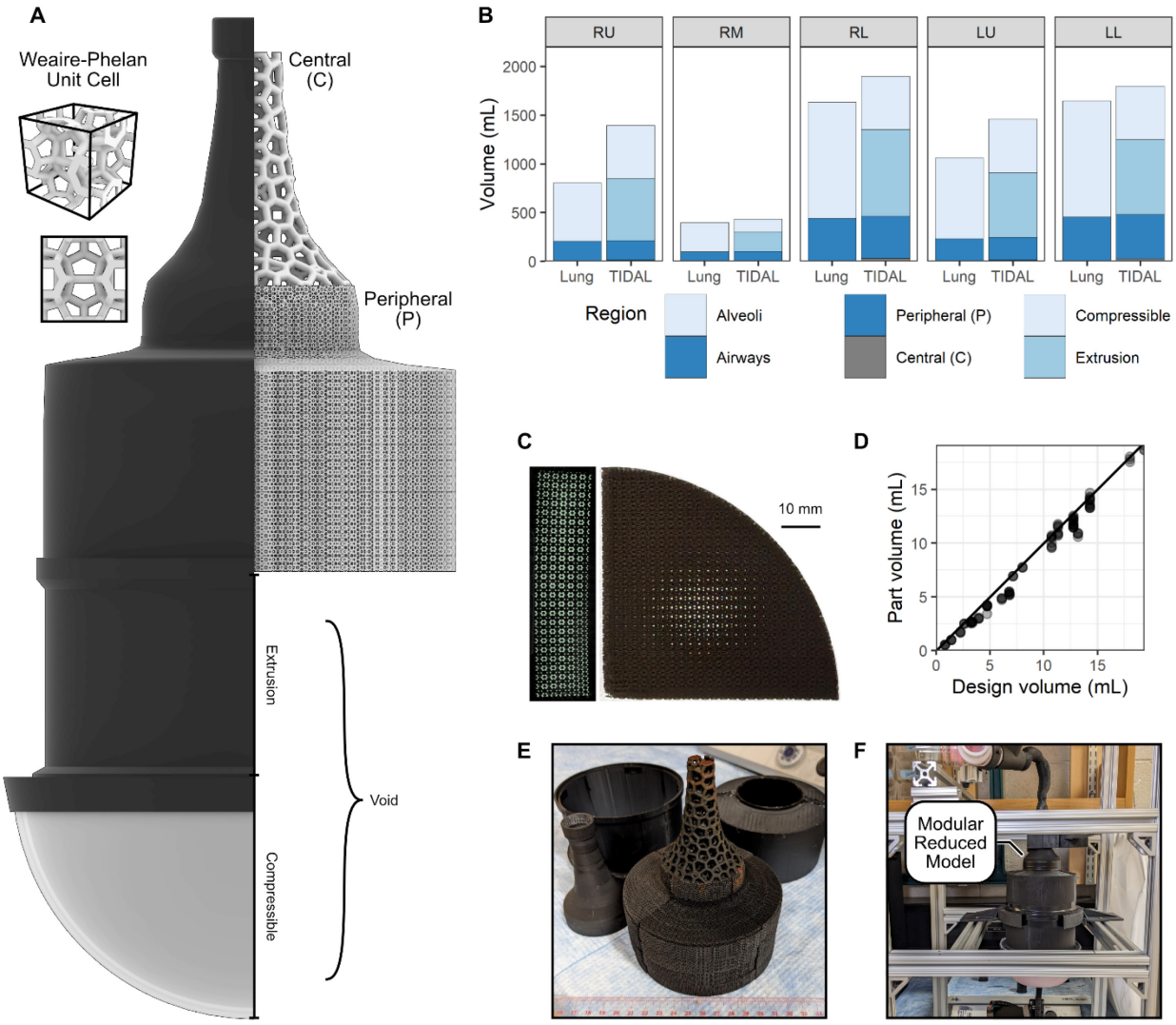

Figure 3. Airway approximation features. (A) Each lobe is approximated by a horn shell derived from the cumulative airway dimensions. The shell is scaled and filled with a porous lattice structure based on the Weaire-Phelan repeat unit cell geometry. (B) Comparison between tabular lung volumes[52] and TIDAL approximation volumes for each lobe. TIDAL regions (Central, Peripheral, Extrusion, Compressible) correspond to void space shown in (A). (C-E) All parts are 3D printed and characterized. (C) X-ray computed tomography slice (left) and visual inspection (right) of a peripheral quarter segment. (D) Part mass converted to volumes are consistent with design features. (E) 3D printed realization of (A) showing components of the LL. (F) The individual lobe can be fitted with upper airway attachments to create a reduced model. See also Tables S2-S7.

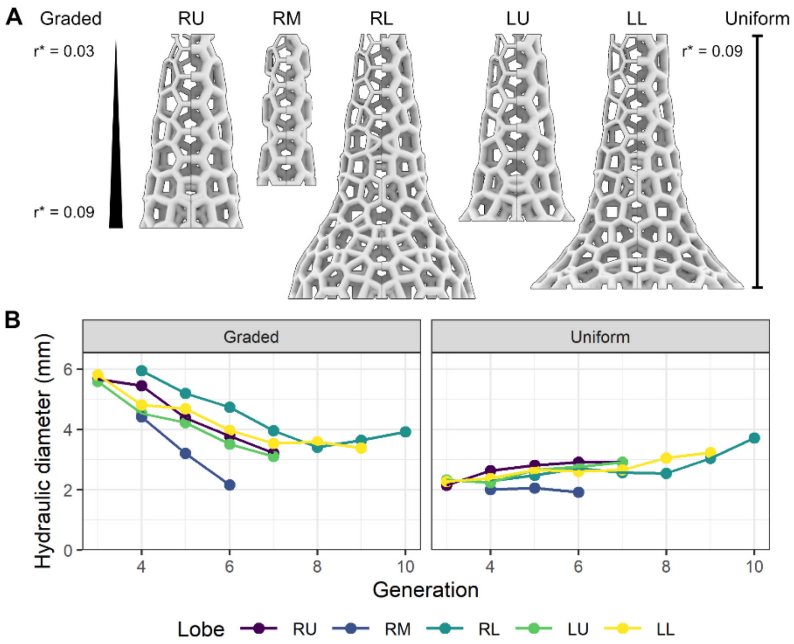

Figure 4. Central lattice designs. (A) Unique central lattice designs for each lobe, including graded (left) and uniform (right) lattice element thickness. (B) Calculated hydraulic diameter of central lattice designs. Graded element thickness results in decreasing average hydraulic diameter along the path length, consistent with trends in airway diameter.

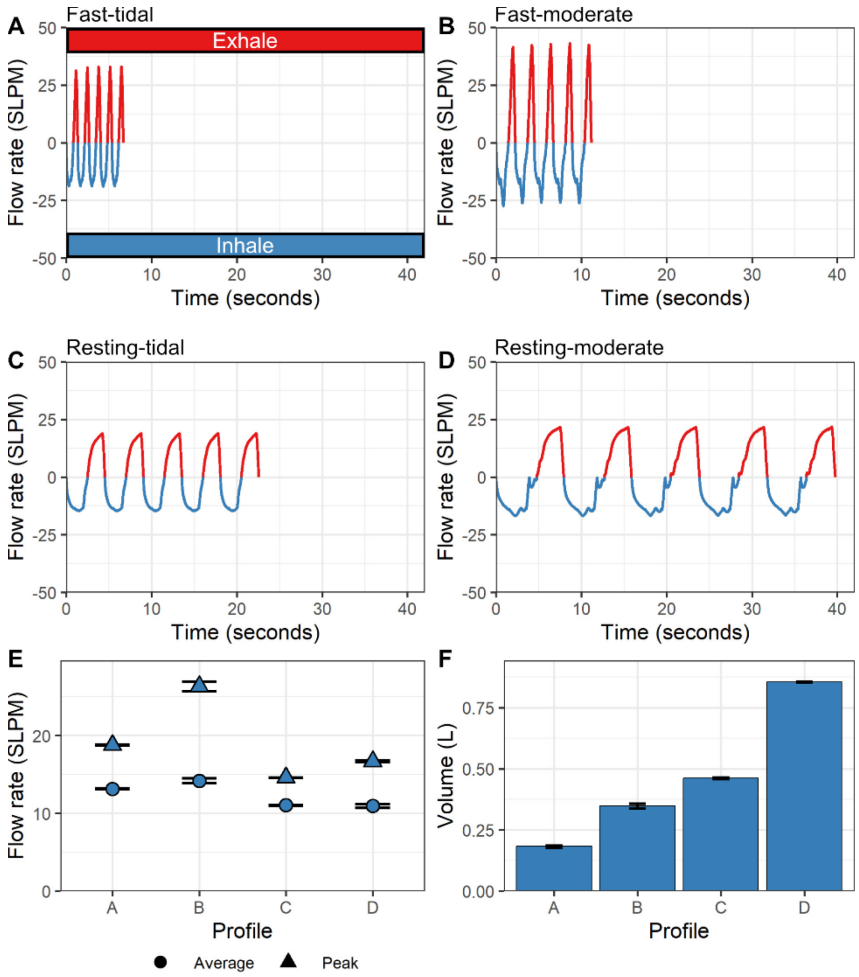

Figure 5. Breathing profiles generated by the complete TIDAL system, corresponding to resting breathing for an adult. (A-D) Breathing waveforms corresponding to fast-tidal, fast-moderate, resting-tidal, and resting-moderate configurations, respectively. (E) Summary of peak and average inhalation flow rates. (F) Summary of inhalation volumes during breathing. Reported as average, where error bars indicate standard deviation (n=5).

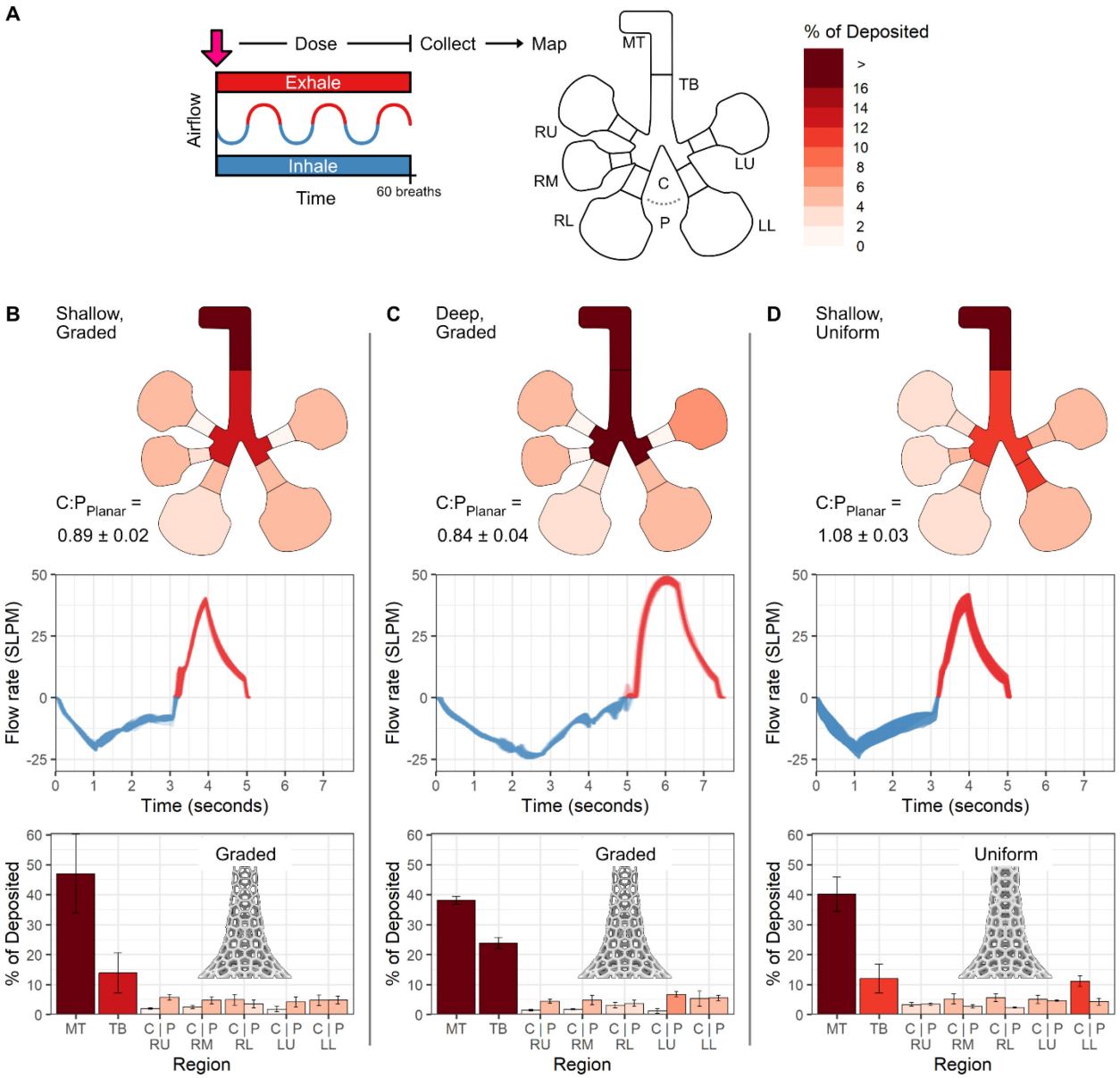

Figure 6. Aerosol deposition maps for three conditions after 60 breaths. (A) The TIDAL model was dosed with fluorescent rhodamine B-loaded aerosol (VMD 6.77 µm) from a vibrating mesh nebulizer for a period of 60 breaths, then disassembled and washed to quantify spatial aerosol deposition for (B) shallow breathing with graded central lattice, (C) deep breathing with graded central lattice units, and (D) shallow breathing with uniform central lattice units. (B-D) Top: average deposition map. The converted planar C:P deposition ratio is shown for each condition (mean ± standard deviation). Middle: overlayed breathing maneuver flow profiles for 24 breaths (A, B) or 28 breaths (C). Bottom: corresponding aerosol deposition as a percentage of mass recovered within the TIDAL model (n=3, mean ± standard deviation). See also Figures S3-S5.

Tables

Table 1. Summary of aerosol deposition experiment breathing conditions and results. Aerosol deposition reported as a percentage of rhodamine B recovered from the TIDAL model components. See also Figures 6, S3-S5.

Breathing maneuver	Shallow	Deep	Shallow
Central lattice design	Graded	Graded	Uniform
Breath volume (mL, standard)	592 ± 19	1068 ± 17	679 ± 123
Peak inspiratory flow rate (SLPM)	19.9 ± 1.0	23.7 ± 0.7	21.5 ± 2.3
Average inspiratory flow rate (SLPM)	11.1 ± 0.4	12.8 ± 0.2	12.7 ± 2.3
Aerosol deposition (%)			
MT	47.0 ± 13.2	38.1 ± 1.3	40.2 ± 5.7
TB	13.9 ± 6.7	23.9 ± 1.9	12.0 ± 4.8
RU	7.8 ± 1.2	5.9 ± 0.4	6.8 ± 0.9
RM	7.3 ± 1.0	6.5 ± 1.7	7.9 ± 2.1
RL	8.5 ± 3.0	6.8 ± 1.3	8.0 ± 1.4
LU	6.0 ± 2.5	8.0 ± 0.8	9.7 ± 1.5
LL	9.6 ± 2.9	10.8 ± 2.8	15.4 ± 2.2
L:R	0.66 ± 0.18	1.0 ± 0.28	1.1 ± 0.11